Review answers for Dr. Balázs Ujvári

1. **Can the scattering muography be used for large object tomography? If yes, under what conditions?**

Scattering muography cannot be used for particularly large objects such as mountains or rock layers, but it can be applied in cases where the examined object can be 'sandwiched' between detectors, such as cargo containers, nuclear reactors, or furnaces. My colleagues have developed a closet-sized instrument (80 cm × 80 cm × 40 cm imaging space) with tracking detectors applied above and below the imaging zone. In the literature, one can find examples of larger sizes as well, for instance, imaging trucks or cargo containers [S. Barnes etal *Instruments* **2023** 7(1)] or even nuclear fuel casks [K. Aymmans etal *IAEA-CN-303-131* (2022)]. The practical limit is the budget for large-size detector development, making it basically impossible to image objects hundreds of meters in size such as mountains or rock layers.

2. **Page 15: when you are talking about "in some cases even up to 5 GeV", is it the muon or the parent particle? If it is the muon, since energy of the primary cosmic particle can be even 10^{20} eV, it can be even higher. In the real measurements what is the origins of these up to 5GeV muons?**

The referenced article [H. Gómez etal *J. Instrum.* **12**: P12018 (2021)] claims, based on simulations, that background can be caused by 'forward scattering muons' in certain geometrical cases, which can be relevant even up to 5 GeV muons (before scattering), as shown in figures below.

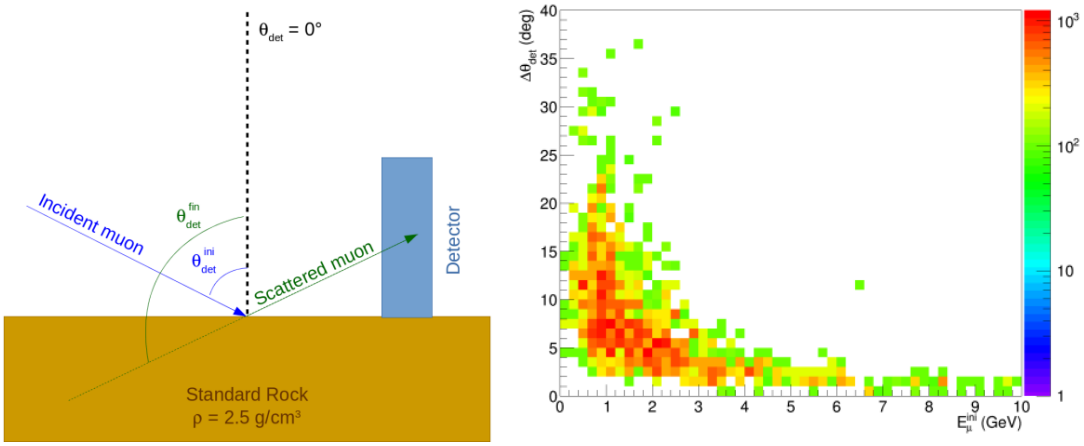

Figure on the left: schematic of scattering of 'forward' muons. Right panel shows the muon energy dependency of zenith angle scattering [H. Gómez etal *J. Instrum.* **12**: P12018 (2021)].

This geometrical case can exist for example around the contour of a mountain object with a hill slope close to arriving muon angle, blurring the edge of the mountain image. Alternatively, if significant amount of material located in front of the detector, muons can scatter there, as the schematics shows below:

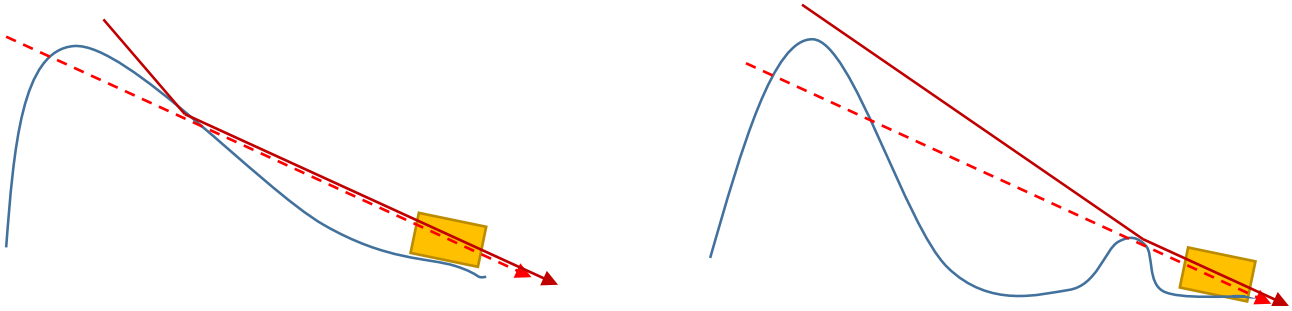

Figures showing possible cases where high energy muon (red) scattering causes background in the detector (yellow rectangle), mimicing signal (dashed).

3. **The borehole detectors were mentioned, how can these small detectors be used for muography?**

My group is developing borehole muography detectors with a modularly expandable concept to ensure desired statistics (active surface). Each module is approximately 10 cm × 100 cm (diameter × length), so three modules have almost the same active surface as MTS modules (which were successfully applied in many underground measurements in 10 – 100 m depths).

I would also note, that in borehole muography the typical targets are large ore bodies or rock layers which have significant average density differences, therefore large angle bins can be used (resulting in more statistics in a given time). The high resolution imaging (eg. exploring small cavities) probably not realistic in boreholes, nevertheless borehole muography could be useful in mineral exploration for the above mentioned reasons.

4. **In the CCC your group used strips, why did you use pick-up wire plane in the AMWPC instead of these strips? What are the main innovations, developed by the CCC, you use in the AMWPC?**

The reason derives from one of the main development goal of the Advanced MWPC which is cost-efficiency, furthermore reliable and robust construction methodology. The practical reason for using wires instead of PCB strips is that manufacturing large-size cathode planes with PAD strips, even with commercial PCB etching technology, it is very expensive and we experienced unreliable quality regarding the flatness of the cathode plane.

The main innovations in the CCC, which later also applied in the AMWPC, are the combination of the following techniques: the readout logic (position information from PAD and Field wires; high voltage and ADC readout in Sense wires), the construction materials (glass-fibered epoxy and two-component epoxy glues, PCBs, brass and tungsten wires), and the application of Ferroline C18 gas (commercial, non-flammable, non-toxic welding shielding gas).

5. **Page 24: what was the trigger conditions for this test? Did you optimize/reset/lower the signal condition to have trigger from the chamber 1, or 4/5 trigger condition solved this problem. Did you change the digital trigger threshold to have track point at the chamber 1, or the original threshold was used before and after the injection?**

The track acceptance condition is usually N-1 chamber hit signal. In this case, 8 chambers were used in the full system and at least 7 signal were required for a track, this way ensuring >99% efficiency. The plots only show 5 chambers (1 reference and 4 contaminated chambers) for simplicity. However, it is important to note that the tracking efficiency in each chamber does not drop; it remains constant. Even a 34% gain drop is tolerable and does not affect tracking efficiency, as claimed in the dissertation, and I also created some plots below to demonstrate this. Therefore, changing the threshold is not necessary and it was not changed during the measurements.

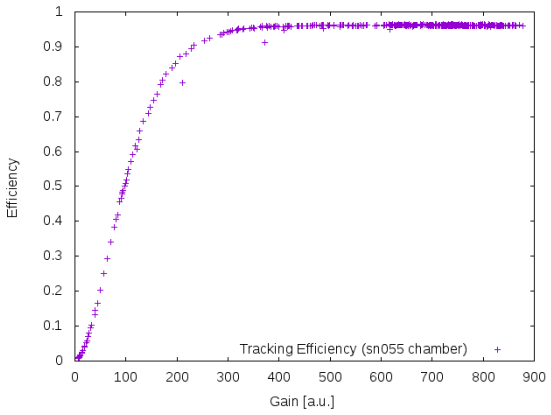

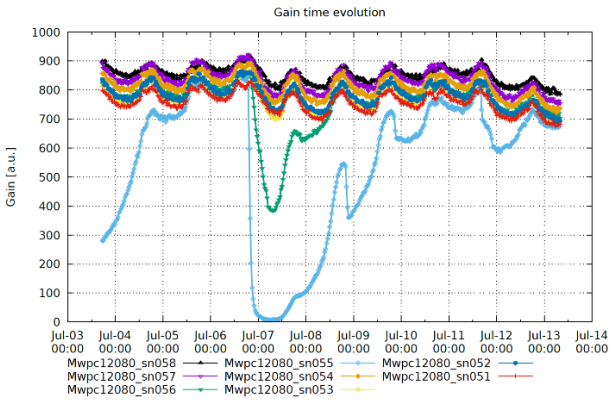

Figures show the tracking efficiency and gain dependencies in case of large gain drops (due to air contamination) in the last chamber of the gas line. Right shows the time dependent gain measurement of eight chambers, showing that the last chamber had air contamination (gain drop). Left is the efficiency depending on the gain, showing that even ~50% gain drop doesn't change the efficiency in the last chamber.

6. **How the tracking algorithm determines the number the position and the width of the lead walls. Describe the tracking algorithm you used here.**

In every case, the basic principle of the default tracking algorithm is the simplest case: least square linear fit to all the selected track points, and check linearity with χ^2 test. I describe some of the track selection and filtering methods in my dissertation (clusters, combinatorial criterion, noise filtering, performance monitoring, fiducial areas) what my colleagues apply in their tracking algorithms. Then the track candidate discarded above a certain level of χ^2 cut (background particle scattering). But the default algorithm does not determine or require the number and position of the lead scattering walls. For this, different algorithm or Monte Carlo simulation required.

There are several ways to reduce background, eg., applying more scattering walls or higher resolution detectors, which both require significant hardware work and cost. Research is also ongoing in various directions to develop the tracking algorithm for better signal-to-noise (and background) ratio in a given detector configuration. My colleagues exploring to extend the χ^2 cut method with examining the angle deviation between different track sections segmented by the lead walls, when there are sufficient number of track points in each section. The idea could be useful not only in background suppression [B. Raboczki, BSc disszertation, ELTE Fizika (2022)], but also in muon scattering tomography [Cs. Botond, OTDK dissertation, ELTE Fizika (2023)]. The former is explained briefly in the figure, right. In this case, there is only one lead wall in the measurement, the angle difference refers to the separately segmented tracking case, and the χ^2 refers to the default tracking (no segmentation). Most of the events, which are the useful signals, are around zero, and the parabolic correlation between the two method is apparent. Research is in progress to apply filtering based on angle deviation, which must be verified by simulation and/or calculations in different muon and background particle energies, angles, and detector configurations.

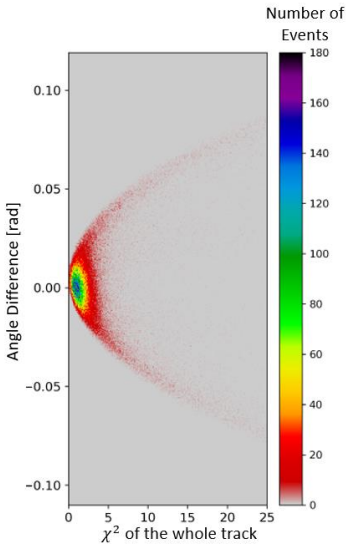

Comparison of Chi-square and angle deviation in case of a lead scattering wall [B. Raboczki (2022)].

There are also efforts to implement detector simulations to optimise lead wall configurations, and track acceptance. For the latter, figures below show the comparison of traditional χ^2 method with different parameters (left), and a new neural network based method (right) depending on the arriving muon energy.

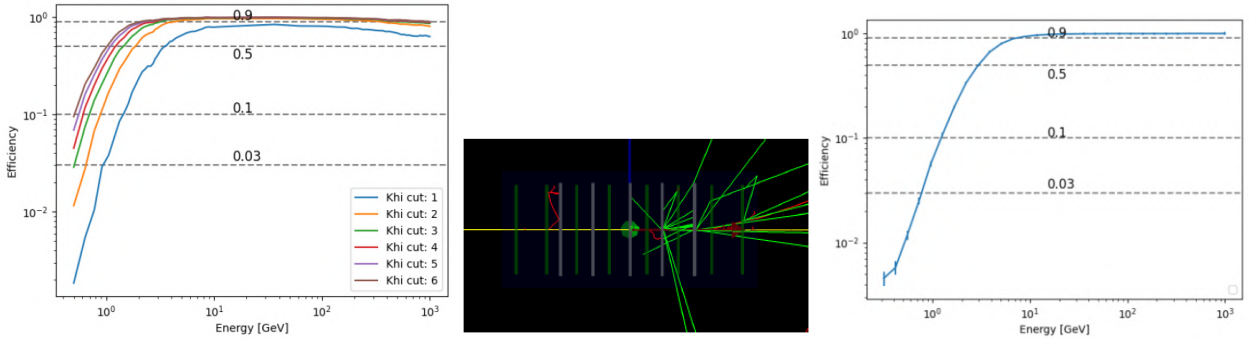

Figures show the results of Gean4 Monte Carlo simulation on SMO detectors (5 x 2 cm lead walls) for examining the energy cut with different traditional χ^2 cut (left), and teaching machine learning algorithm to predict track acceptance (right) [G. Galgoczi, PhD dissertation 1. thesis point, ELTE (2023)].

7. **In the paper: High Efficiency Gaseous Tracking Detector for Cosmic Muon Radiography, Fig 5 shows the signal amplitudes by 5/6 and 6/6 trigger conditions. The gauss shape of the peak at 5/6 trigger condition suggests one chamber is not working at all, because no signal is coming out, all I see is noise. What can be the reason? If a chamber gives a lower than average signal, this peak should have different shape.**

The cited figure can be seen below. In case of 5/6 track combinatorial track condition, the curve continues with a Landau signal (after the Gauss shape) which implies that there are signals originate from track hits,

not only noise. However, there are ADC signals (in the Gauss region) which correspond to events when the track did not cross the detector, or not the sensitive part, eg., crossed an inner support, therefore no primer electron reaches the Sense Wire and no electron avalanche created. The track condition allows this scenario. In this case, when the DAQ reads the ADC from this chamber, it is only electronic noise. It is very useful information, since by this measurement, we can ensure that the signal above Detection Level is almost certainly not electric noise.

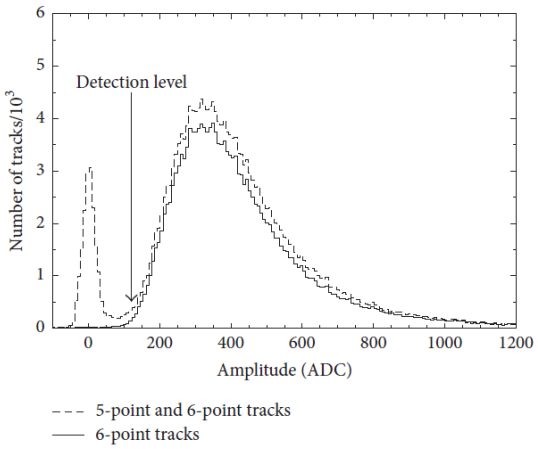

8. **Fig 3.36: the post-amplifier seems to be not CCC, can you create a scaled plot? If the bottom of the GEM is not grounded, how it changes the parameters of this post-amplifiers? Did you used the field wires and strips (if it's a CCC) for validating the avalanche positions?**

A scaled plot is shown in the figure below. This implies the asymmetric arrangement of the wire plane. However, this detector is terminologically not just a CCC, but a TCPD, so I would discuss the parameters uniquely since it contains a GEM which alters the electric field and the functionality. The GEM acts as a "pre-amplifier" between the drift region (the upper Cathode – GEM part), and the post-amplification (GEM – wire plane). We implemented separate high voltage channels for the Cathode wires, GEM top, GEM bottom, Field wires, and Sense wires. The latter is positive and all the others on negative potential. The high voltage on the GEM bottom (post-amplification side) is typically a few hundred volts higher than on the GEM top. This voltage difference ensures that electrons will pass (and amplified) through the GEM holes, and subsequent amplification occurs again around the Sense wire.

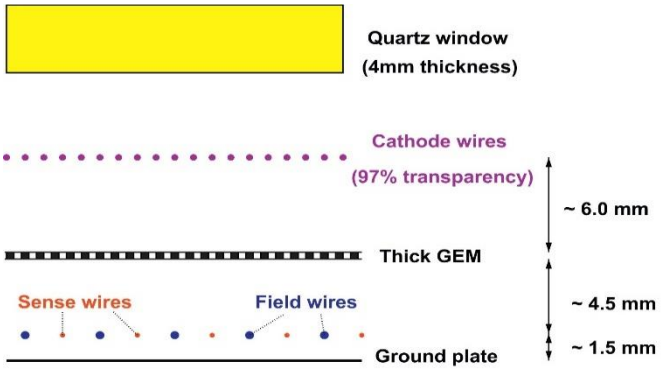

Figure shows the realistic scaled schematic cross-section of the Leopard [G. Hamar and D. Varga, NIM **694** 16-23 (2012)].

Using Field wires and strips to acquire position information is crucial for Cherenkov ring detection. However, for the Leopard system, we didn't use it since the position resolution information from the stepper motors are orders of magnitude more accurate. In those TCPDs where the PAD channel readout is implemented, it would be indeed an interesting study to perhaps guide the Leopard position calibration with coordinate readout.

9. **Fig 3.40: What was the exact configuration in this measurement? You mentioned it was above the detector, does it mean above the GEM foil?**

The extra wires, for focus calibration, were place on top of the Quartz window, outside the detector. Therefore, when the optical system focuses on a wire, the UV photons are mostly reflected and do not get inside the detector, leading to a PE yield drop. In the other cases, photons reach the GEM surface (somewhere) which creates photoelectron. Note that in this case, we are not interested where the avalanche created; the information only indicates that the optical system is not focusing on the wire. This measurement provides a simple and very accurate focal distance measurement, and since we know the exact distance from these calibration wires to the GEM surface, we can align the optical system easily to the GEM surface for the gain scan measurements.

10. **Page 85: you are talking about the uncertainty of the ML-EM method. Is it the statistical or systematical uncertainty? Why can't we say anything about the uncertainty by this method?**

I intended to express that Eq. (4.15) does not include calculations for either statistical or systematic uncertainties. The Eq. (4.15) ML-EM algorithm is derived from emission tomography and it is a statistical method[1] based on the Poisson distribution of photon detection from a radioactive isotope concentration distribution $p(n_i) = \frac{N_i^{n_i} e^{-N_i}}{n_i!}$, where n_i is a count number in the ith measurement, $N_i = E(n_i)$ is the expected count number which is also the variance. However, I applied this algorithm by substituting density for isotope concentration and giving density-length to the algorithm instead of count rates (therefore, linearizing the original transmission tomography problem of muography). To put it simply: emission tomography gives lesser uncertainty where the concentration is high, but in muography it is the opposite, higher density results lesser statistics.

The statistical uncertainty must be calculated in a different way, this is solved later in Eq. (4.17, 4.18, 4.19) for the Bayes method[2]. Systematic uncertainties of the flux calculation (Sec. 4.1.3) can be included (adds up squarely in Eq. 4.12) if there is a reliable estimation, this is under research. The bias of the density estimate (Fig. 4.16 left) is also a systematic error which is also under research. Applying transmission tomography directly, using muon counts as inversion input, could be also studied. These are interesting research directions for the future.

---

[1] In the EM (Expectation Maximization) step we calculate the expectation of $p(\boldsymbol{s};\boldsymbol{x}) = \prod\prod \frac{E(s_{im})^{s_{im}} \cdot e^{-E(s_{im})}}{E(s_{im})!}$, where $n_i = \sum_m^M s_{im}$ and $E(s_{im}) = F_{im} \cdot x_m$ (**F** is the system matrix and **x** is the concentration distribution). In the ML (Maximum Likelihood) step we calculate $\partial_x \ln p(\boldsymbol{s};\boldsymbol{x}) = 0$. More details in lecture notes of D. Légrády p48-53: https://dtk.tankonyvtar.hu/xmlui/handle/123456789/7835

[2] Actually, ML-EM can also integrate Bayes criterion: $\rho_k^{n+1} = \rho_k^n \frac{1}{\sum_i^N F_{ik} + \partial_i p(x)} \frac{\sum_i^N \varrho_i F_{ik}}{\sum_m^M F_{im} \rho_m^n}$, where $\partial_i p(x)$ is the *a priori*, this method is called MAP-EM (Maximum Aposteriori Expectation Maximization)

11. Fig 4.10: What are the reasons of those artifacts? Do these shadow lines come from the method?

Yes, they come from the method. In Fig. 4.10 left, it can be seen that the artifact lines start from detectors and crosses the cavity in “star-shape”. These lines are not real density anomalies, but arise due to the Bayes criterion, and the lack of information, eg., imperfect mapping (discretization error) between voxel grid and measurement bins, underdetermination, limited detector positions and resolution. Bayes criterion causes the cavity to blur (not significantly) along lines: the higher criterion penalizes very different results from the estimate, but it is necessary to regulate the solution. In the middle panel, statistical uncertainties are simulated, which makes the image noisy but still significant at the cavity. In the right panel, the propagated standard deviation map also points out the inhomogeneous statistics (orange vs blue regions).

12. Fig 4.14: Are those lines anomalies or real lower density areas?

In our terminology, we call all the real lower (or higher) density regions ‘anomalies’, which are lower (or higher) than the geologically expected average density. If the inversion results in a lower (or higher) density anomaly which is not real but an error of the method (as discussed in the previous question), we call them ‘artefacts’. The weight $\mathbf{W}_{\rho}^{(0)}$(and covariance $\mathbf{C}_{\rho}^{(1)}$) matrices provide support for the estimation of significance of the results. Below 1.8 g/cm^3, the results are not only significant, but even the core drills validated the existence of the low-density zone. We cannot be sure about the dark-green regions, but the significant low-density zones in the inversion results refer to unique-shape contiguous crack zones in 3D (and doesn’t follow “star-shape”), so this also lowers the chance for them to be artefacts.